Astrocytic and neuronal oxidative metabolism are coupled to the rate of glutamate-glutamine cycle in the tree shrew visual cortex

Article *in* Glia · November 2017

DOI: 10.1002/glia.23259

7 authors, including:

Sarah Sonnay
École Polytechnique Fédérale de Lausanne
19 PUBLICATIONS **418** CITATIONS
SEE PROFILE

Jordan Poirot
Université de Fribourg
4 PUBLICATIONS **38** CITATIONS
SEE PROFILE

Nathalie Just
French National Institute for Agriculture, Food, and Environment (INRAE)
66 PUBLICATIONS **479** CITATIONS
SEE PROFILE

Gregor Rainer
Université de Fribourg
103 PUBLICATIONS **6,097** CITATIONS
SEE PROFILE

Received: 18 July 2017 | Revised: 20 October 2017 | Accepted: 24 October 2017

DOI: 10.1002/glia.23259

GLIA
WILEY

RESEARCH ARTICLE

Astrocytic and neuronal oxidative metabolism are coupled to the rate of glutamate–glutamine cycle in the tree shrew visual cortex

Sarah Sonnay[1] | Jordan Poirot[2] | Nathalie Just[3] | Anne-Catherine Clerc[1] | Rolf Gruetter[1,4,5] | Gregor Rainer[2] | João M. N. Duarte[1,6,7]

[1]Laboratory for Functional and Metabolic Imaging (LIFMET), Ecole Polytechnique Fédérale de Lausanne (EPFL), Lausanne, Switzerland

[2]Department of Medicine, Visual Cognition Laboratory, University of Fribourg, Fribourg, Switzerland

[3]University Hospital Münster, Münster, Germany

[4]Department of Radiology, University de Lausanne, Lausanne, Switzerland

[5]Department of Radiology, University de Geneva, Geneva, Switzerland

[6]Department of Experimental Medical Science, Faculty of Medicine, Lund University, Lund, Sweden

[7]Wallenberg Centre for Molecular Medicine, Lund University, Lund, Sweden

Correspondence
João M. N. Duarte, Department of Experimental Medical Science, BMC C11, Sölvegatan 19, SE-221 84 Lund, Sweden.
Email: joao.duarte@med.lu.se

Abstract

Astrocytes play an important role in glutamatergic neurotransmission, namely by clearing synaptic glutamate and converting it into glutamine that is transferred back to neurons. The rate of this glutamate–glutamine cycle (V_{NT}) has been proposed to couple to that of glucose utilization and of neuronal tricarboxylic acid (TCA) cycle. In this study, we tested the hypothesis that glutamatergic neurotransmission is also coupled to the TCA cycle rate in astrocytes. For that we investigated energy metabolism by means of magnetic resonance spectroscopy (MRS) in the primary visual cortex of tree shrews (*Tupaia belangeri*) under light isoflurane anesthesia at rest and during continuous visual stimulation. After identifying the activated cortical volume by blood oxygenation level-dependent functional magnetic resonance imaging, ^{1}H MRS was performed to measure stimulation-induced variations in metabolite concentrations. Relative to baseline, stimulation of cortical activity for 20 min caused a reduction of glucose concentration by -0.34 ± 0.09 μmol/g ($p < 0.001$), as well as a $-9\% \pm 1\%$ decrease of the ratio of phosphocreatine-to-creatine ($p < 0.05$). Then ^{13}C MRS during [1,6-^{13}C]glucose infusion was employed to measure fluxes of energy metabolism. Stimulation of glutamatergic activity, as indicated by a 20% increase of V_{NT}, resulted in increased TCA cycle rates in neurons by 12% (V_{TCA}^{n}, $p < 0.001$) and in astrocytes by 24% (V_{TCA}^{g}, $p = 0.007$). We further observed linear relationships between V_{NT} and both V_{TCA}^{n} and V_{TCA}^{g}. Altogether, these results suggest that in the tree shrew primary visual cortex glutamatergic neurotransmission is linked to overall glucose oxidation and to mitochondrial metabolism in both neurons and astrocytes.

KEYWORDS

^{13}C, cortical energy metabolism, fMRI, MRS, stimulation

Abbreviations: Ace, acetate; ADP, adenosine diphosphate; Ala, alanine; ANOVA, analysis of variance; Asc, ascorbate; Asp, aspartate; ATP, adenosine triphosphate; BOLD, blood oxygenation level-dependent; CMR_{glc}, cerebral metabolic rate of glucose; Cre, creatine; CRLB, Cramér-Rao lower bound; EPI, echo-planar imaging; fMRI, functional magnetic resonance imaging (fMRI); FE, fractional enrichment; GABA, γ-aminobutyrate; GE, gradient echo; Gln, glutamine; Glu, glutamate; GSH, glutathione; Gly, glycine; GPC, glycerophosphorylcholine; Glc, glucose; Ins, *myo*-inositol; Lac, lactate; MR, magnetic resonance; MRS, MR spectroscopy; NAA, *N*-acetylaspartate; NAAG, *N*-acetylaspartylglutamate; PE, phosphorylethanolamine; PCho, phosphorylcholine; PCre, phosphocreatine; scyllo, *scyllo*-inositol; T_2^*, effective time constant of transverse magnetisation; Tau, taurine; TCA, tricarboxylic acid; tCho, total choline-containing compounds; tCr, total creatine; TR, repetition time; TE, echo time; VOI, volume of interest.

1 | INTRODUCTION

The mammalian brain has high energy demands, primarily met by high oxidative metabolism in mitochondria, which are important for reversing ion fluxes underlying synaptic transmission and action potential signaling in neurons (Attwell & Laughlin, 2001). Over the last two decades, the investigation of brain energy metabolism *in vivo* with preserved cellular interactions has among others relied on magnetic resonance (MR) spectroscopy (MRS) techniques along with administration of ^{13}C-labeled tracers (Lanz, Gruetter, & Duarte, 2013). Namely, MRS

studies upon infusion of ^{13}C-enriched glucose revealed that focal activation of the rat cortex results in increased tricarboxylic acid (TCA) cycle flux (V_{TCA}) together with increased cerebral metabolic rates of glucose (CMR_{glc}) and oxygen (CMR_{O2}; Hyder *et al*., 1996, 1997; Yang & Shen, 2006). Glutamatergic activity has been considered to be coupled to glucose oxidative metabolism of neurons in the living brain, with minor involvement of astrocytic mitochondria (Hyder & Rothman, 2012). Although the contribution of astrocytes for whole brain energy metabolism has long been underestimated, there are reports of increased oxidative metabolism in astrocytes in response to somatosensory stimulation (Chuquet, Quilichini, Nimchinsky, & Buzsáki, 2010; Cruz, Lasater, Zielke, & Dienel, 2005; Dienel, Schmidt, & Cruz, 2007; Sonnay, Duarte, Just, & Gruetter, 2016). Astrocytes are part of the so-called tripartite synapse, and actively integrate and fine-tune synaptic signaling (Volterra & Meldolesi, 2005). Astrocytes also surround capillaries and participate in blood flow regulation (Gordon, Choi, Rungta, Ellis-Davies, & MacVicar, 2008), contributing to the control of glucose and oxygen delivery from the blood stream.

While data from many laboratories confirmed that the rate of neuronal oxidative metabolism is coupled to that of the glutamate–glutamine cycle that represents glutamatergic neurotransmission (reviewed in Hyder & Rothman, 2012), it remains to be ascertained whether the rate of oxidative metabolism in astrocytes is effectively coupled to neurotransmission.

Technical developments in ^{13}C MRS methods at high magnetic field, coupled to state-of-the-art metabolic modeling, allowed to investigate fluxes of energy metabolism in neurons and astrocytes with high precision, namely in small animals (Lanz *et al*., 2013). However, the non-invasive study of activity-induced stimulation of metabolic networks by ^{13}C MRS, which requires long experimental paradigms, has been limited by the ability to deliver prolonged stimuli in a continuous manner. In anesthetized rodents, somatosensory stimulation paradigms result in a reduced blood oxygenation level-dependent (BOLD) functional magnetic resonance imaging (fMRI) signal 15–20 min after stimulation onset, likely due to neuronal and hemodynamic adaptations that can be mitigated with presentation of intermittent stimuli (discussed in Sonnay, Just, Duarte, & Gruetter, 2015). In contrast, continuous and prolonged visual stimulation may be achievable by randomly delivering alternating patterns. The tree shrew (*Tupaia belangeri*) is a day-active non-primate mammal possessing a relatively large primary visual cortex (V1; Sesma, Casagrande, & Kaas, 1984), characterized by specific orientation columns and direction selectivity (Bosking, Crowley, & Fitzpatrick, 2002), as well as temporal and spatial frequency selectivity (Van Hooser, Roy, Rhodes, Culp, & Fitzpatrick, 2013; Veit, Bhattacharyya, Kretz, & Rainer, 2011). The hemispheric representation of the visual space is moreover highly conserved in the tree shrew V1 (Drenhaus, Rager, Eggli, & Kretz, 2006).

Therefore, the aim of the present study was to take advantage of the well-developed tree shrew V1 to characterize stimulation-induced metabolic adaptations using ^{1}H MRS and ^{13}C MRS along with [1,6-^{13}C]glucose infusion at high magnetic field (14.1 T). In the present study, the measurement of labeling transference from [1,6-^{13}C]glucose into all aliphatic carbons of glutamate, glutamine and aspartate allowed to determine metabolic fluxes in both neurons and astrocytes. Therefore, we tested the hypothesis that the rate of oxidative metabolism in astrocytes is coupled to that of glutamatergic neurotransmission.

2 | MATERIALS AND METHODS

2.1 | Animal preparation

All experiments were performed under the Swiss federal law on animal experimentation, and were approved by the local authority (EXPANIM-SCAV).

Adult 0.5–6.6 years-old tree shrews (*Tupaia belangeri*; 7 females and 2 males) weighing 218±16 g were randomly allocated to experimental groups: stimulation ($n = 5$) and rest ($n = 4$). Tree shrews were housed at University of Fribourg, in 6 m^3-cages equipped with climbing, hiding and sleeping places. At most five animals were placed in the same cage. The room temperature was kept at 26 ± 1°C, the humidity was 50% ± 15%, and the light-dark cycle had 12 hr of light starting at 8:00 a.m. Animals received food pellets and water every day (*ad libitum*), and additional fruits were given once or twice a week.

On the day of the experiment, at 6:00 a.m., the tree shrews were transported in their nest boxes to the laboratory in Lausanne. Then, to avoid stress, they were initially induced with 4% isoflurane (Animalcare, York, UK) vaporized in 30% oxygen in N_2O delivered into the next box. A mixture of ketamine (50 mg/kg i.m.; Graeub, Bern, Switzerland) and xylazine (0.8 mg/kg i.m.; Graeub), and an atropine solution (0.02 mg/kg i.m.; Sintetica, Mendrisio, Switzerland) were injected in the left and right posterior legs, respectively, while isoflurane was discontinued. A tracheotomy was then performed, pancuronium bromide (Sigma-Aldrich, Buchs, Switzerland) was administered i.p. (initial dose of 0.4 mg/kg, then 0.2 mg/kg every 45 min), and the animal was mechanically ventilated with a pressure-driven ventilator (MRI-1, CWE Ardmore, PA). Ventilation was initially set to a volume of 2–2.5 mL and a rate of 100 breaths/min. Catheterization of the femoral vein and artery of the left hind leg was then performed under 1.2%–1.5% isoflurane. After surgery, isoflurane was reduced to 0.5%–0.7%, and the animal was placed in a home-built holder with ear and mouth inserts for head fixation.

A drop of 5 mg/mL atropine (PharmaciePlus, Bulle, Switzerland) was applied to the eyes for pupil dilation. Animals wore Boston ES-UV rigid gas permeable contact lenses (+96 D; diameter of 7 mm, base curve radius of 3.8 mm, front curve radius of 2.45 mm; Hecht Contactlinsen GmbH, Freiburg, Germany) to compensate for their −4D emmetropic refractive state at a focal distance of 1 cm (Norton, Wu, & Siegwart, 2003).

Heart rate, arterial blood pressure, body temperature, and breathing rate were monitored through the arterial catheter with an animal monitoring system (SA Instruments, Stony Brook, NY). Body temperature was regulated with a warm water circulation system based on the feedback obtained from a rectal temperature probe (SA Instruments). Arterial pH and pressures of O_2 (P_aO_2) and CO_2 (P_aCO_2) were measured using the Cobas b121 analyzer (Roche Diagnostics, Rotkreuz, Switzerland) and were maintained at normal levels by adjusting

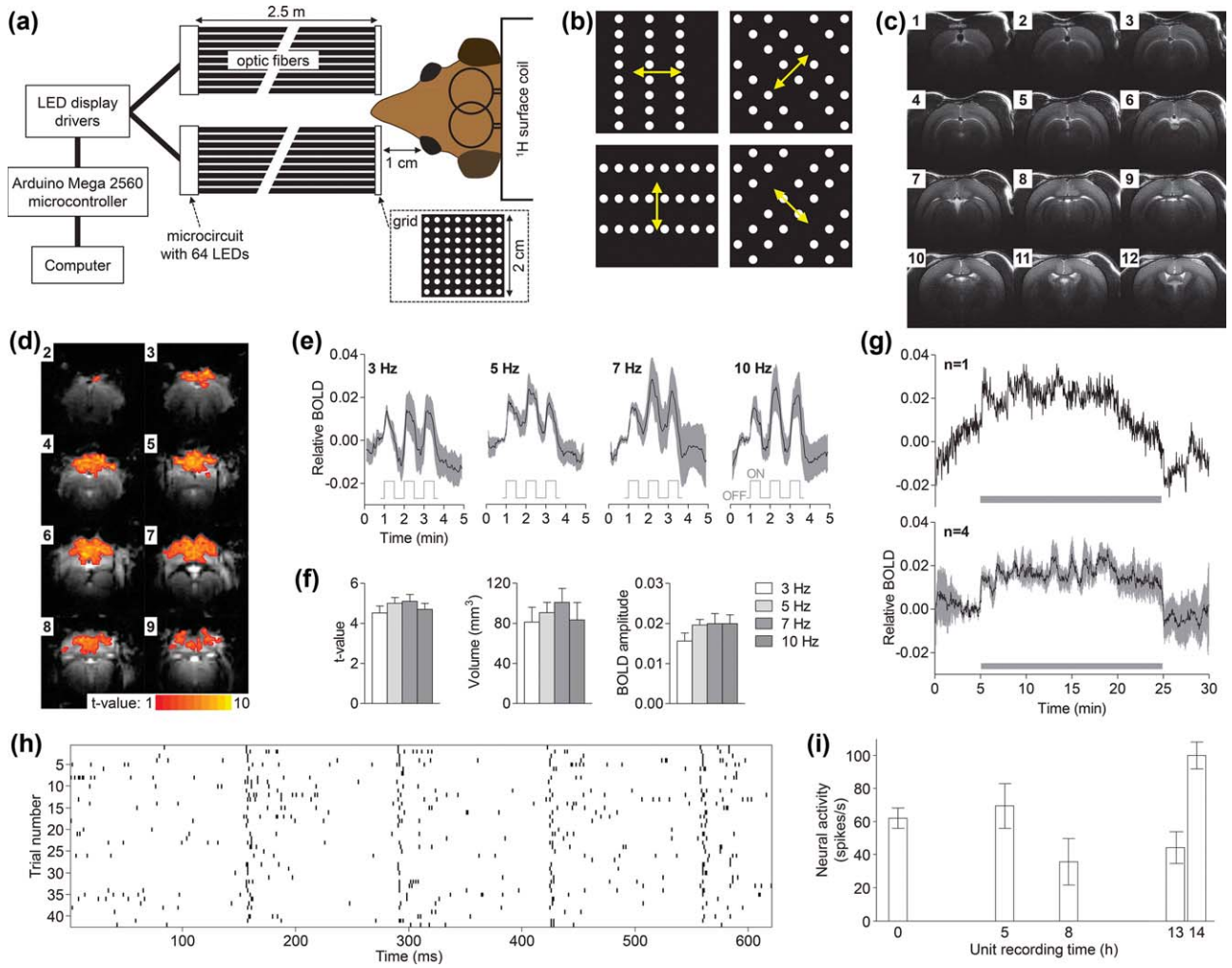

FIGURE 1 Experimental set-up for visual stimulation in the scanner (a) and examples of delivered patterns (b). T_2-weighted images with slice thickness of 0.8 mm were used as anatomical reference in BOLD fMRI and MRS experiments (c). Slices numbered 1–12 follow the direction caudal to rostral. (d) Typical activation *t* value map overlaid on 0.8-mm thickness GE-EPI images showing typical V1 activation following the paradigm 30 sec ON – 30 sec OFF at 5 Hz. (e) Relative BOLD responses at 3–10 Hz following the stimulation paradigm represented by the grey trace. (f) Average *t* value, activation volume and relative BOLD amplitude calculated from (e). (g) Sustained V1 activation for 20 min in four animals upon continuous visual stimulation with randomly switched moving lines at 5 and 7 Hz, and in alternating directions. Horizontal grey bars indicate the stimulation period. (h) Example single neuron action potential recording on 42 repetitions of a 7-Hz visual flicker stimulus, showing entrainment of neuronal activity to visual flicker transients. (i) Bar plot showing robust visually driven activity in five neurons recorded over the course of 14 hr in response to the 7-Hz visual flicker stimulus, demonstrating stable and robust V1 neuronal activation. Data are mean ± *SEM* [Color figure can be viewed at wileyonlinelibrary.com]

respiratory rate and volume. In case of pH drop at normal P_aCO_2, sodium bicarbonate (Sigma-Aldrich) was infused at a maximum dose of 3 mmol/kg/h from a 3.75% (w/v) solution.

For ^{13}C MRS, [1,6-^{13}C]glucose (99.9% ^{13}C in both carbons; Sigma-Aldrich) was infused to achieve a constant fractional enrichment (FE) throughout the experiment (Duarte, Lanz, & Gruetter, 2011). Plasma samples were collected for FE determination.

All infused solutions were prepared in 0.9% (w/v) NaCl.

2.2 | Visual stimulation

Visual stimulation was performed binocularly with a home-built MR-compatible device composed of two microcircuits, each containing 64 white light-emitting diodes (LED) with 1.75 mm^2 of lightened surface (Farnell, Zug, Switzerland), and spaced by 1.1 mm. The microcircuits were located outside the magnet bore, and LEDs were connected by 2.5-m long optic fibers to two non-magnetic 2-cm squared grids placed at 1 cm from the animal's eyes (Figure 1a). The microcircuits were interfaced via 8-digit LED display drivers to an Arduino Mega 2560 microcontroller (Play-zone GmbH, Cham, Switzerland) that was connected via universal serial bus to a computer for power source and for loading stimulation paradigms, which were coded in C language and loaded before the experiment.

Visual stimulation was performed by randomly delivering frames with lines in four orientations (*i.e.*, two diagonals, horizontal and vertical), drifting in either direction at a spatial frequency of 0.04–0.05

cycle/degree (Figure 1b). Temporal frequencies of 3–5-7–10 Hz were used for V1 activation mapping. In prolonged stimulation paradigms, frames were presented with random temporal frequencies of 5 or 7 Hz, which elicit strong firing rates in cortical layers 4 and 2/3 (Van Hooser *et al.*, 2013). Frames were randomly switched every 5 sec. The display contrast was set to maximum in order to achieve maximal BOLD response (Liang *et al.*, 2013), and resulted in a luminosity of 45–50 LUX for all presented patterns.

2.3 | Electrophysiological experiments

To verify robust electrophysiological signal over many hours, an additional animal was anaesthetized and artificially ventilated as described above, and then was prepared as detailed in Veit, Bhattacharyya, Kretz, & Rainer (2014). The animal was placed in a stereotaxic device that permitted visual stimulation using a 21-inch cathode ray tube monitor positioned at 40 cm from the animal, using Psychophysics Toolbox running on a Mac mini computer for visual stimulus delivery. Neuronal activity was recorded using tungsten electrodes (FHC, Bowdoin, ME) with ~1 MΩ impedance at 1 kHz. Signal were amplified and digitized at 24 kHz sampling rate using a RZ5 system (Tucker-Davis Technologies, Alachua, FL).

2.4 | MRI and MRS

Experiments were performed on a 14.1 T/26 cm horizontal bore magnet (Magnex Scientific, Abingdon, UK), equipped with 12-cm gradients (400 mT/m in 120 μs) and interfaced to a Direct Drive console (Agilent Technologies, Palo Alto, CA). MRI and ^{1}H MRS were performed with a quadrature transmit/receive surface coil resonating at 600 MHz. For ^{13}C MRS the coil was a geometrically decoupled combination of a ^{1}H quadrature surface coil and a ^{13}C linearly polarized surface coil. The brain was placed at the isocenter of the magnet, and T_2-weighted fast spin echo images were acquired with repetition time (TR) of 4 s and echo time (TE) of 40 ms for anatomical reference. Shimming was performed with FAST(EST)MAP (Gruetter & Tkác, 2000).

BOLD fMRI was performed using a single shot gradient echo (GE)-echo planar imaging (EPI) sequence (TR = 2 sec, TE = 18 ms; field of view of 23 × 23 mm^2; matrix of 64 × 64; bandwidth of 200 kHz; 8 slices with 0.8-mm thickness). Images were reconstructed using home-built MATLAB routines (MathWorks, Natick, MA). Motion correction was performed using SPM8 (Statistical Parametric Mapping, London, UK). No other correction or filtering methods were applied. Activation *t* value maps were computed on a voxel-wise basis from the comparison between the experimental data and the applied paradigm schemes using STIMULATE (Strupp, 1996), as previously described (Sonnay *et al.*, 2015). Time courses from the voxels within the activated volume were used to calculate mean relative BOLD responses.

^{1}H MRS was performed using SPECIAL with TR = 4 sec and TE = 2.8 ms (Mlynárik, Gambarota, Frenkel, & Gruetter, 2006) in a volume of interest (VOI) of 35 μL (2.2 × 4 × 4 mm^3) localized in V1, within the area of activation assessed by BOLD fMRI. Spectra were acquired continuously during three consecutive series of 320 scans (21.3–min each) that corresponded to baseline, stimulation, and recovery periods. Spectra were saved in blocks of four scans, frequency corrected to compensate for B_0 drift by aligning the creatine peak at 3.03 ppm, and summed in blocks of either 64 or 160 scans corresponding to 4.3 min and 10.7 min, respectively. Metabolite concentrations were determined with LCModel (Stephen Provencher Inc., Oakville, Ontario, Canada), including a macromolecule (Mac) spectrum in the database and using the unsuppressed water signal measured from the same VOI (eight scans) as internal reference (Mlynárik *et al.*, 2006). Water content was set to 80% of the tissue, as in rodents (Duarte, Do, & Gruetter, 2014 and references therein).

^{13}C spectra were acquired using the semi-adiabatic DEPT combined with 3D-ISIS ^{1}H localization (Henry, Tkác, & Gruetter, 2003a) in a VOI of 105 μL (3 × 7 × 5 mm^3) also localized in V1. Spectra were saved in sums of 126 scans (~5.3 min). Visual stimulation was started 10 min before [1,6-^{13}C]glucose infusion to achieve metabolic steady-state. Spectral analysis was performed using LCModel (Henry, Oz, Provencher, & Gruetter, 2003b). At the end of each experiment, animals were euthanized using a focused microwave fixation device (Gerling Applied Engineering, Modesto, CA) at 4 kW for 2.2 sec. The portion of the visual cortex corresponding to the VOI was dissected. Cortical tissue and plasma samples were stored at −80°C until further processing. Water soluble metabolites were extracted with 7% (v/v) perchloric acid. Then, samples were dried, re-dissolved in $^{2}H_2O$ (99.9%, ^{2}H, Sigma-Aldrich), and ^{1}H and ^{13}C spectra were acquired on a DRX-600 spectrometer equipped with a 5-mm cryoprobe (Bruker BioSpin SA, Falländen, Switzerland) as previously described (Duarte, Cunha, & Carvalho, 2007). FE in amino acid carbons measured in cortical extracts served to scale the ^{13}C curves measured *in vivo* (Duarte & Gruetter, 2013).

2.5 | Metabolic modeling

Metabolic fluxes were estimated by fitting the mathematical model of energy metabolism with two compartments—neurons and glia—described previously (Sonnay, Duarte, Just, & Gruetter, 2017b). The glial compartment can be assumed to account mainly for astrocytic metabolism, as this glial cell type is the most metabolically active (Amaral, Hadera, Tavares, Kotter, & Sonnewald, 2016). The distinction between neuronal and astrocytic metabolic fluxes relies on the assumption that pyruvate carboxylase and glutamine synthetase are exclusively present in astrocytes, that most glutamate resides in neurons, and on the ability to measure the different labeling incorporation into carbons 2 and 3 of both glutamate and glutamine, which is generated via pyruvate carboxylation to oxaloacetate (Sonnay, Gruetter, & Duarte, 2017c). Analysis of labeling incorporation was performed separately for glucose and amino acids to reduce flux correlations and thus improve estimation reliability (Duarte *et al.*, 2011).

Glucose transport and consumption were analyzed by fitting both dynamic and steady-state MRS data with a reversible Michaelis-Menten model (Duarte & Gruetter, 2012). For this analysis, the contribution of plasma glucose to the measured signal was subtracted assuming a blood volume in the brain of 31 μL/g (at rest) and 34 μL/g (during

stimulation), as reported for the rat cortex under isoflurane anesthesia (Kim, Hendrich, Masamoto, & Kim, 2007). The fit of the model to the relation of cortex-to-plasma glucose concentrations at steady-state allowed to estimate the apparent Michaelis constant of glucose transport (K_t), which was then used in the analysis of glucose labeling curves, thus determining the apparent maximum transport rate (T_{max}) and cerebral metabolic rate of glucose (CMR_{glc}).

The two-compartment model was then fitted to the ^{13}C enrichment curves of all aliphatic carbons of glutamate, glutamine and aspartate. A time resolution of 5.3 min (128 scans) was used for glutamate C4, C3 and C2, and glutamine C4 and C3, while a resolution of 10.6 min (256 scans) was preferred for glutamine C2 and aspartate C3 and C2 to achieve sufficient signal-to-noise ratio for reliable quantification. The determined fluxes were the apparent glutamatergic neurotransmission (*i.e.* glutamate-glutamine cycle, V_{NT}), neuronal and astrocytic TCA cycle ($V_{TCA}{}^n$ and $V_{TCA}{}^g$), pyruvate carboxylase (V_{PC}), exchange between TCA cycle intermediates oxaloacetate and 2-oxoglutarate ($V_X{}^n$ and $V_X{}^g$ in neurons and astrocytes, respectively), as well as dilution fluxes at the level of pyruvate (V_{in}), astrocytic acetyl-CoA (V_{dil}) and astrocytic glutamine (V_{ex}). Calculated fluxes included the glutamine synthetase rate ($V_{GS} = V_{NT} + V_{PC}$), the fraction of the astrocytic TCA cycle that results in full oxidation of glucose ($V_g = V_{TCA}{}^g - V_{PC}$), the oxidative fraction of CMR_{glc} that is $CMR_{glc(ox)} = (V_{TCA}{}^n + V_{TCA}{}^g + V_{PC})/2$, and the loss of pyruvate from the cortical parenchyma was $V_{out} = 2 \times CMR_{glc} - 2 \times CMR_{glc(ox)} + V_{in}$.

2.6 | Statistics

Data are mean ± *SEM* unless otherwise stated. The effect of visual stimulation on metabolite concentrations (from ^1H MRS) was analyzed with repeated measures one-way ANOVA followed by Tuckey post-tests. Modeling of labeling curves were firstly performed with the curves from each animal. The effect of visual stimulation on the set of metabolic fluxes was analyzed by two-way ANOVA followed by individual Student *t* tests. Then, based on the range of V_{NT} the data were separated into two groups—either low or high V_{NT}—and the resulting group average turnover curves were fitted again. In this case, flux variance was obtained by Monte Carlo analysis (Duarte *et al*., 2011). The effect of stimulation on this set of fluxes was assessed by permutation analysis, followed by individual two-tailed Student *t* tests (Sonnay *et al*., 2016, 2017b). In case of multiple comparisons, *p* values were corrected with the Holm-Bonferroni method. All calculations included error propagation.

3 | RESULTS

To map cortical activity, T_2-weighted images were acquired for anatomical reference (Figure 1c), and V1 activation was then identified in *t* value maps representing stimulation-induced BOLD signal variations (Figure 1d). Cortical activity was mapped based on continuous visual stimuli delivered at constant spatial frequency, but different temporal frequencies with the paradigm [30 sec ON – 30 sec OFF], repeated for three blocks (Figure 1e). The volume of activation, mean *t* value, and BOLD response amplitude were similar for all frequencies used (Figure 1f). Namely, stimulation-induced BOLD signal increase ranged between 1.6% ± 0.6% and 2.0% ± 0.6%. Since cortical BOLD response did not vary significantly with stimulation frequency, prolonged stimulation paradigms were performed with random presentation of frames with lines drifting at either 5 or 7 Hz. Sustained BOLD signal increase during stimulation was often masked by relatively large baseline fluctuations, which are probably associated to the usage of light isoflurane anesthesia (0.5%–0.7%). BOLD responses were not observable at the higher isoflurane dose of 1% (not shown). Nevertheless, a sustained BOLD response was noticeable during a 20-min stimulation in four experiments (Figure 1g), and the mean response amplitude was 1.8% ± 0.1% above baseline (before the stimulation).

We further verified in a separate experiment outside the MR scanner that in the experimental conditions of this study, robust neuronal activity was observed in V1 over the course of many hours. An example dataset is shown in Figure 1h, demonstrating reliable neuronal action potentials to a 7-Hz flickering stimulus, with each visual flicker stimulus triggering action potentials in a typical neuron recorded at the beginning of the experiment. Figure 1i shows that similar robust unit activity was obtained during recordings of additional units later during the experiment, up to 14 hours in the case of this example session. This demonstrates that our experimental preparation elicits robust activation of V1 circuits, which can reliably persist over the course of many hours.

To determine stimulation-induced changes of metabolite concentrations, ^1H spectra were acquired in the tree shrew cortex from a VOI placed in the region of intense activation (Figure 2a). Simulated spectra of 21 metabolites were initially included in the LCModel basis set, and fitted to data collected during the baseline (Figure 2b). Phosphorylcholine, alanine, *scyllo*-inositol, ascorbate and acetate consistently presented Cramér-Rao lower bound (CRLB) values above 30%, and thus could not be reliably quantified. Alanine, *scyllo*-inositol, ascorbate and acetate were therefore excluded from the LCModel basis set for time course analyses, and phosphorylcholine and glycerophosphorylcholine were reported as their sum (*i.e*., total choline).

Due to sporadic motion, we excluded 5 spectra in experiment #4, 2 in experiment #7, and 2 in experiment #9 from all 240 spectra saved. In addition, one experiment (#6) was excluded from the ^1H MRS analysis, because of linewidth degradation (30% increase in linewidth) during the acquisition. Lactate was undetectable in another experiment (#5).

Changes in metabolite concentrations over time were assessed in V1 at temporal resolutions of 4.3 (Figure 2a), as well as 10.7 min. Figure 2c shows the metabolite time courses, as well as the phosphocreatine-to-creatine ratio (PCr/Cr) and total creatine (Cr + PCr), with temporal resolutions of 4.3 and 10.7 min. We found significant alterations in the levels of glucose ($F_{7,26} = 2.96$, $p < 0.01$) and in PCr/Cr ($F_{7,26} = 2.06$, $p < 0.05$). A significant decrease in glucose concentration occurred during stimulation, reducing by −0.34 ± 0.9 μmol/g in the second half of the stimulation period ($p < 0.001$ *vs*. baseline), which recovered when stimulation ceased. Sixteen minutes after stimulation onset PCr/Cr significantly decreased by 9 ± 1% ($p < 0.05$ *vs*. baseline). No other concentration changes reached statistical significance.

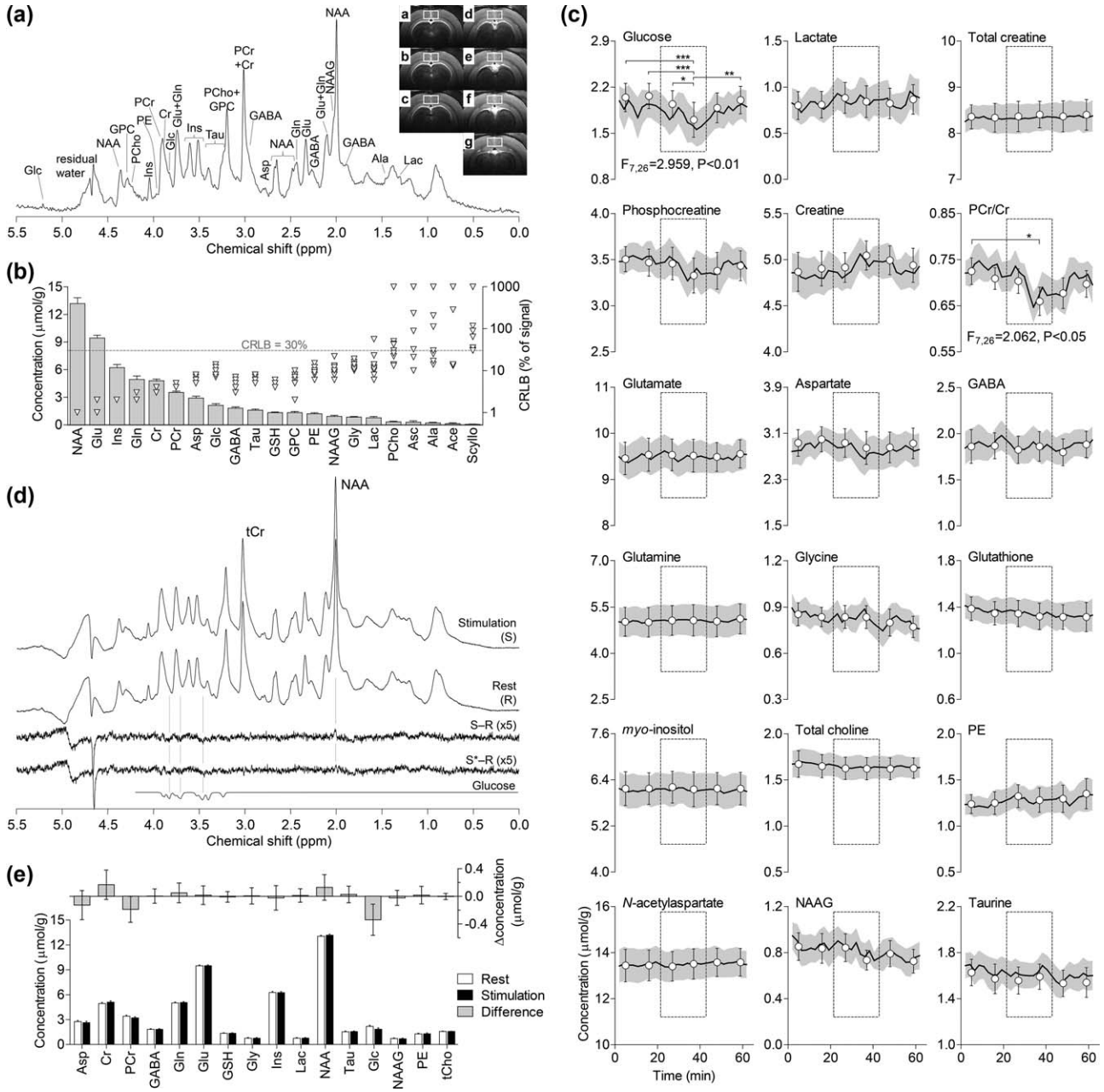

FIGURE 2 (a) Typical ^{1}H spectrum at 14.1 T acquired during 4.3 min from the tree shrew V1. The VOI is overlaid on the displayed T_2-weighted images (0.6-mm thickness; slices a–g follow the direction caudal-rostral). Gaussian apodization was applied before Fourier transformation (gf = 0.08, gfs = 0.02) for resolution enhancement. (b) Concentrations (bars, mean ± *SEM* of $n = 9$) and CRLB values (triangles) resulting from LCModel analysis with the fit of 21 metabolite spectra in the basis set. (c) Time courses of metabolite concentrations during baseline, stimulation and recovery. The neurochemical profile was quantified in spectra summed from 64 (solid line) or 160 scans (open circles), equivalent to temporal resolutions of 4.3 and 10.7 min, respectively. The stimulation period is depicted by the dashed box. Data are mean ± *SEM* of $n = 8$, and $n = 7$ for lactate, and were analyzed with repeated measures ANOVA on the 4.3-min time resolution. Tukey's tests were used for post-hoc comparisons on the 10.7-min time resolution: $^{*}p < 0.05$, $^{**}p < 0.01$, $^{***}p < 0.001$. (d) Spectra of the second half of the stimulation (S) and rest (R) periods summed over eight animals (displayed with 1-Hz line broadening). Their subtraction (S – R) shows a clear *N*-acetylaspartate (NAA) signal at 2.01 ppm due to the BOLD effect on the linewidth. Additional 10% line broadening for stimulation (1.1 Hz) results in a reduction of NAA but still an observable residual that corresponds to glucose in the subtracted spectrum (S* – R). Subtracted spectra are shown with five-fold larger vertical scale (×5). Glucose spectrum is shown for comparison. (e) Metabolite concentrations resulting from LCModel analysis of these summed rest (R) and stimulation (S) spectra. Error bars represent CRLB. Animal #6 was excluded due to linewidth deterioration during acquisition. Abbreviations: Ace, acetate; Ala, alanine; Asc, ascorbate; Asp, aspartate; Cre, creatine; GABA, γ-aminobutyrate; Gln, glutamine; Glu, glutamate; GSH, glutathione; Gly, glycine; GPC, glycerophosphorylcholine; Glc, glucose; Ins, *myo*-inositol; Lac, lactate; NAA, *N*-acetylaspartate; NAAG, *N*-acetylaspartylglutamate; PE, phosphorylethanolamine; PCho, phosphorylcholine; PCre, phosphocreatine; scyllo, *scyllo*-inositol; Tau, taurine; tCho, total choline-containing compounds

TABLE 1 Physiology parameters and plasma concentrations of lactate and glucose before and after ^{1}H and ^{13}C MRS experiments. Data are mean ± *SEM*

	^{1}H MRS		^{13}C MRS	
	Before	**After**	**Before**	**After**
pH	7.35 ± 0.02	7.39 ± 0.02	7.42 ± 0.01	7.38 ± 0.01
P_aCO_2 (mm Hg)	41.6 ± 1.2	40.7 ± 1.9	36.9 ± 1.1	34.3 ± 1.1
P_aO_2 (mm Hg)	141 ± 8	136 ± 8	136 ± 3	139 ± 4
O_2 saturation (%)	99.1 ± 0.1	98.9 ± 0.2	99.0 ± 0.1	99.0 ± 0.1
Blood pressure (mm Hg)				
Systole	213 ± 11	208 ± 12	197 ± 9	181 ± 7
Diastole	134 ± 10	125 ± 12	109 ± 10	94 ± 7
Heart rate (bpm)	404 ± 12	410 ± 14	393 ± 7	398 ± 7
Temperature (°C)	37.2 ± 0.1	37.2 ± 0.2	37.1 ± 0.1	36.9 ± 0.1
Lactate (mmol/L)	1.4 ± 0.3	1.6 ± 0.3	1.8 ± 0.3	4.0 ± 0.5
Glucose (mmol/L)	7.3 ± 0.9	6.4 ± 0.4	5.8 ± 0.3	23.6 ± 2.0

The last 160 spectra acquired during either baseline or stimulation were summed over eight animals and analyzed with LCModel. The linewidth narrowing caused by the increase in T_2^* (effective time constant for the decay of transverse magnetization) due to the BOLD effect was noticeable in the methyl resonance of *N*-acetylaspartate at 2.01 ppm of the subtracted spectrum (Figure 2d). This effect on peak linewidths further confirms activation of V1 during stimulation, and was minimized by a 10% increase in line broadening applied to the summed spectrum acquired during activation. Note that the reduction of glucose signals during stimulation can be observed in the resulting difference spectrum from the negative resonances between 3.4 and 3.9 ppm (corresponding to the chemical shifts of glucose protons bound to carbons 2–5). In addition, LCModel analysis of the summed rest and stimulation spectra also indicated concentration changes induced by stimulation comparable to those observed by analyzing spectra from individual experiments (see above): −0.34 μmol/g for glucose, −0.19 μmol/g for phosphocreatine, and +0.17 μmol/g for creatine (Figure 2e).

Plasma glucose levels were similar before and after ^{1}H MRS, as well as other physiology parameters (Table 1), and it is thus unlikely that they influence the measured neurochemical changes.

To assess cortical energy metabolism, ^{13}C MRS was performed during infusion of [1,6-^{13}C]glucose, which resulted in increased plasma glucose concentration and stable FE over the entire acquisition (Figure 3a). At the end of the experiment, FE of glucose C1 in the plasma was 63% ± 1%, whereas plasma lactate C3 and acetate C2 reached 36% ± 2% and 15% ± 4%, respectively. In these conditions, labeling of glucose, glutamate, glutamine, and aspartate was detected in the tree shrew V1 (Figure 3b,c). In the cortical extracts, glucose C1, lactate C3, alanine C3, and acetate C2 had FE of 63% ± 1%, 58% ± 2%, 53% ± 4%, 4% ± 2%, respectively.

To determine glucose transport and metabolism, cortical glucose concentration was measured as a function of plasma glucose at steady-state, which resulted in K_t = 2.6 ± 5.7 mmol/L for all animals (Figure 4a). This K_t value was then used to constrain the fit of dynamic ^{13}C curves from each tree shrew (Figure 4b). The glucose labeling curves were fitted for the first 2 hr of infusion, because the largest glucose variations occurred within the first 15 min after infusion onset. For animals at rest and under stimulation, respectively, T_{max} was 2.6 ± 0.4 and 3.2 ± 0.5 μmol/g/min ($p > 0.1$), and CMR_{glc} was 0.71 ± 0.08 and 1.06 ± 0.33 μmol/g/min ($p > 0.1$).

To determine the alteration of metabolic fluxes in neurons and astrocytes during stimulation, the two-compartment model was fitted to the labeling curves of each tree shrew (Figure 4c). Visual stimulation impacted the set of metabolic fluxes determined by ^{13}C MRS ($F_{1,49}$ = 11.0, p = 0.002, Figure 4d). Flux magnitude was responsible for most variation in the data ($F_{6,49}$ = 101, $p < 0.001$) but did not interact with the stimulation effect ($F_{6,49}$ = 0.653, $p > 0.1$). Post-tests revealed a significant increase of V_{NT} (p = 0.023), V_g (p = 0.019) and $V_{TCA}{}^g$ (p = 0.049). The resulting fluxes were plotted as a function of V_{NT} (Figure 4e). Notably there was a linear relationship between V_{NT} and $CMR_{glc(ox)}$ (slope: 0.97 ± 0.25, p = 0.006), $V_{TCA}{}^n$ (slope: 1.11 ± 0.51, p = 0.065), $V_{TCA}{}^g$ (slope: 0.80 ± 0.22, p = 0.008), V_g (slope: 0.77 ± 0.38, p = 0.082) and V_{GS} (slope: 1.03 ± 0.19, p = 0.001), but not V_{PC} (slope: 0.03 ± 0.19, $p > 0.1$). At V_{NT} = 0, $CMR_{glc(ox)}$ was 0.25 ± 0.05, $V_{TCA}{}^n$ was 0.34 ± 0.11, $V_{TCA}{}^g$ was 0.10 ± 0.05, V_g was 0.04 ± 0.08, V_{GS} was 0.06 ± 0.04, and V_{PC} was 0.06 ± 0.04 (all in μmol/g/min).

To confirm these stimulation-induced modifications in metabolic fluxes, we further analyzed group averaged labeling curves. We noted that one stimulated animal exhibited a neurotransmission rate (V_{NT}) in the range of the rest group (#6, Figure 4e). Therefore, ^{13}C MRS experiments were split in two based on their V_{NT} for metabolic modeling of averaged labeling curves. Experiment #2 was shorter due to physiological deterioration after 160 min and was thus excluded from this analysis. The model was fitted to curves averaged from experiments with V_{NT} below (Group A) and above (Group B) 0.21 μmol/g/min, which is the median V_{NT} of the eight animals (Figure 5a,b).

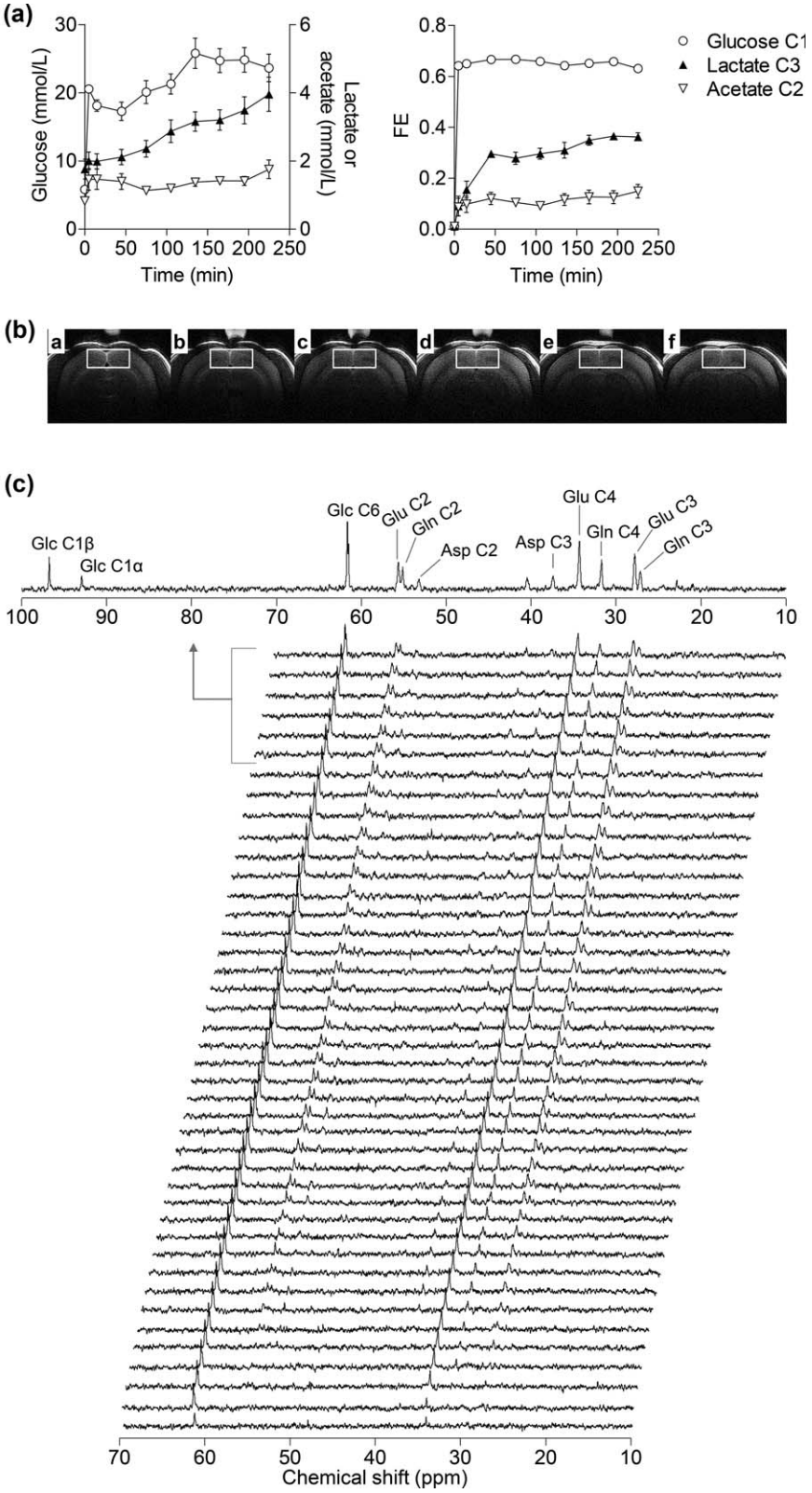

FIGURE 3 (a) Plasma concentration and FE of glucose, lactate and acetate during ^{13}C MRS. (b) Representation of the VOI for ^{13}C MRS in anatomical images of the tree shrew (0.8-mm thickness; slices a to g follow the direction caudal-rostral). The sphere over the head is the [^{13}C]formic acid reference used for radiofrequency pulse calibration. (c) Typical ^{13}C spectra acquired during [1,6-^{13}C]glucose infusion and visual stimulation. Each spectrum is the sum of 128 scans (~5.3 min). In the top is shown the sum of the last 6 spectra. For resolution enhancement, 7-Hz Lorentzian apodization was applied. Abbreviations: Glc, glucose; Glu, glutamate; Gln, glutamine; Asp, aspartate

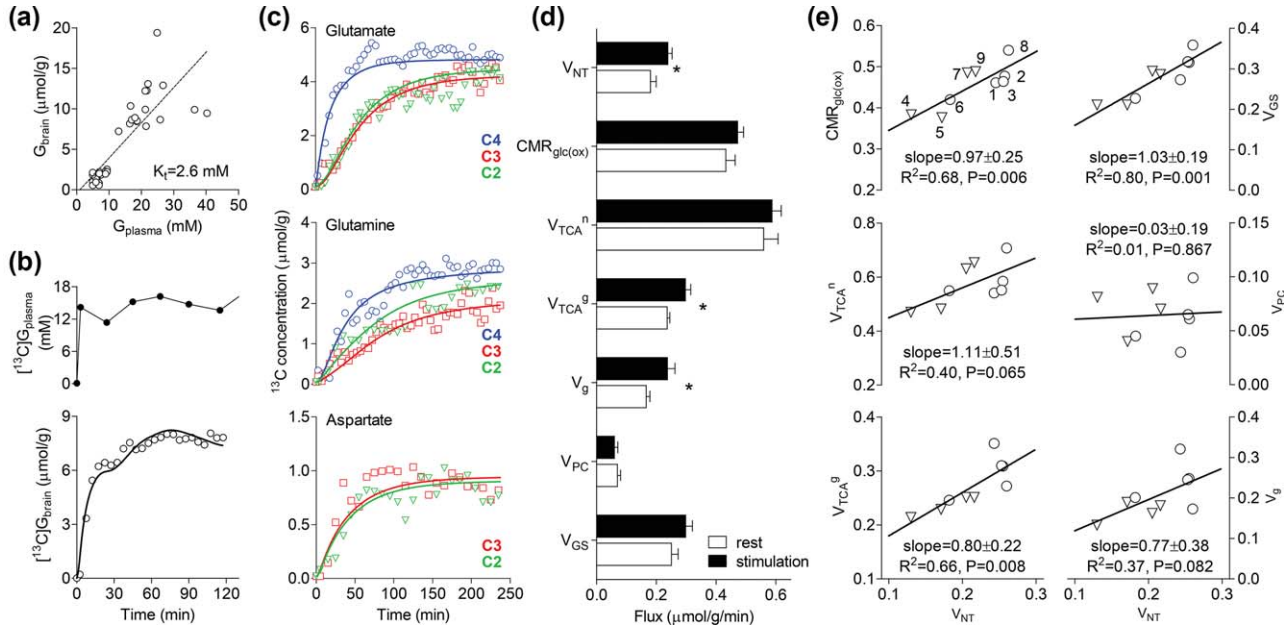

FIGURE 4 Metabolic flux analysis. (a) Analysis of brain glucose transport using steady-state plasma and brain glucose concentrations (G_{plasma} and G_{brain}, respectively) measured before [1,6-^{13}C]glucose infusion and when G_{plasma} was stable for at least 1 hr. Both resting and stimulated animals are pooled together. Data before [1,6-^{13}C]glucose infusion were taken both at rest and during stimulation. During infusion, two steady-state time points were taken for each animal, except for animal #2 that only has one data point. (b) Typical $[^{13}C]G_{brain}$ and $[^{13}C]G_{plasma}$ curves over 120 min and the best fit of the dynamic model. (c) Typical labeling incorporation into aliphatic carbons (symbols) of glutamate, glutamine and aspartate (in μmol/g), and model's best fit (lines). (d) Fluxes of energy metabolism and glutamate–glutamine cycle (in μmol/g/min; mean ± *SEM* of $n = 4$–5) for tree shrews in stimulation and rest groups. $^*p < 0.05$ for rest versus stimulation. (e) Relation between V_{NT} and other metabolic fluxes. Data points represent individual experiments (numbered in top-left plot) from stimulation (circles) and rest (triangles) groups. R^2, slope and *p* value for deviation from zero are shown for each linear regression [Color figure can be viewed at wileyonlinelibrary.com]

Analysis of the glucose labeling curves from Groups A ($f = 68.7$, $R^2 = 0.904$) and B ($f = 351$, $R^2 = 0.980$) resulted in T_{max} of 3.5 ± 0.6 and 3.4 ± 0.3 μmol/g/min ($p > 0.1$) and CMR_{glc} of 1.03 ± 0.19 and 1.29 ± 0.11 μmol/g/min ($p = 0.009$), respectively. Since K_t was associated with a large uncertainty, we tested its effect on parameter determination (Figure 5a). K_t influenced the value of T_{max} but was devoid of major impact on CMR_{glc}.

The two-compartment model of energy metabolism described well the averaged turnover curves of both groups (A: $f = 799$ and $R^2 = 0.950$; B: $f = 945$ and $R^2 = 0.957$; Figure 5b). For Group A, V_{NT} was 0.19 ± 0.02 μmol/g/min and V_{GS} was 0.27 ± 0.02 μmol/g/min; the total rate of cortical glucose oxidative metabolism $CMR_{glc(ox)}$ was 0.43 ± 0.02 μmol/g/min; the fluxes through the TCA cycles in neurons ($V_{TCA}{}^n$) and in astrocytes ($V_{TCA}{}^g$) were 0.52 ± 0.02 and 0.26 ± 0.03 μmol/g/min, respectively; V_{PC} was 0.074 ± 0.008 μmol/g/min (Table 2). Faster oxidative metabolism was observed in Group B relative to Group A (Figure 5c; Table 2). In particular, we estimated faster V_{NT} ($\Delta V_{NT} = 0.038 \pm 0.042$ μmol/g/min, +20% ± 22%, $p = 0.090$, and $p = 0.013$ prior correction), $V_{TCA}{}^n$ ($\Delta V_{TCA}{}^n = 0.061 \pm 0.032$ μmol/g/min, +12% ± 6%, $p < 0.001$) and $V_{TCA}{}^g$ ($\Delta V_{TCA}{}^g = 0.063 \pm 0.057$ μmol/g/min, +24% ± 20%, $p = 0.010$). In Group B, the fraction of $V_{TCA}{}^g$ that represents full oxidation of pyruvate was larger by 38% ± 27% than in Group A ($\Delta V_g = 0.071 \pm 0.052$ μmol/g/min, $p = 0.002$), but V_{PC} was similar. Compared to A, Group B had also larger dilution at the level of acetyl-CoA ($\Delta V_{dil} = 0.079 \pm 0.061$ μmol/g/min, +63% ± 50%, $p = 0.002$). $CMR_{glc(ox)}$ was larger in Group B by +14% ± 7% ($\Delta CMR_{glc(ox)} = 0.058 \pm 0.032$ μmol/g/min, $p < 0.001$). No change was observed for the two groups in V_{ex}, $V_X{}^n$, and $V_X{}^g$, which were associated with large uncertainty (Figure 6a). The uncertainty of these exchange fluxes was nevertheless devoid of substantial impact in the estimation of the remaining fluxes.

To reduce the correlation between the estimated fluxes, the model was fitted separately to the ^{13}C curves of glucose and of amino acids (Duarte *et al*., 2011). After estimating CMR_{glc}, the resulting value was fixed in the modeling of amino acid labeling curves. We verified that CMR_{glc} was devoid of substantial effect on the estimated fluxes (Figure 6b). However, a larger CMR_{glc} was associated with a larger net pyruvate efflux, calculated as $V_{out} - V_{in} = 2 \times CMR_{glc} - 2 \times CMR_{glc(ox)}$.

Tree shrews of both genders were included in the study, and their age varied from 0.5 to 6.6 years (Table 3). Nevertheless, age and gender were homogeneously distributed across the experimental groups (Table 4). Among all estimated metabolic parameters, we found that age was correlated with $V_{TCA}{}^n$ (Pearson $r = -0.71$, uncorrected $p = 0.033$).

4 | DISCUSSION

This study demonstrates that, like neurons, astrocytes stimulate their oxidative metabolism during increased cortical activity in the tree

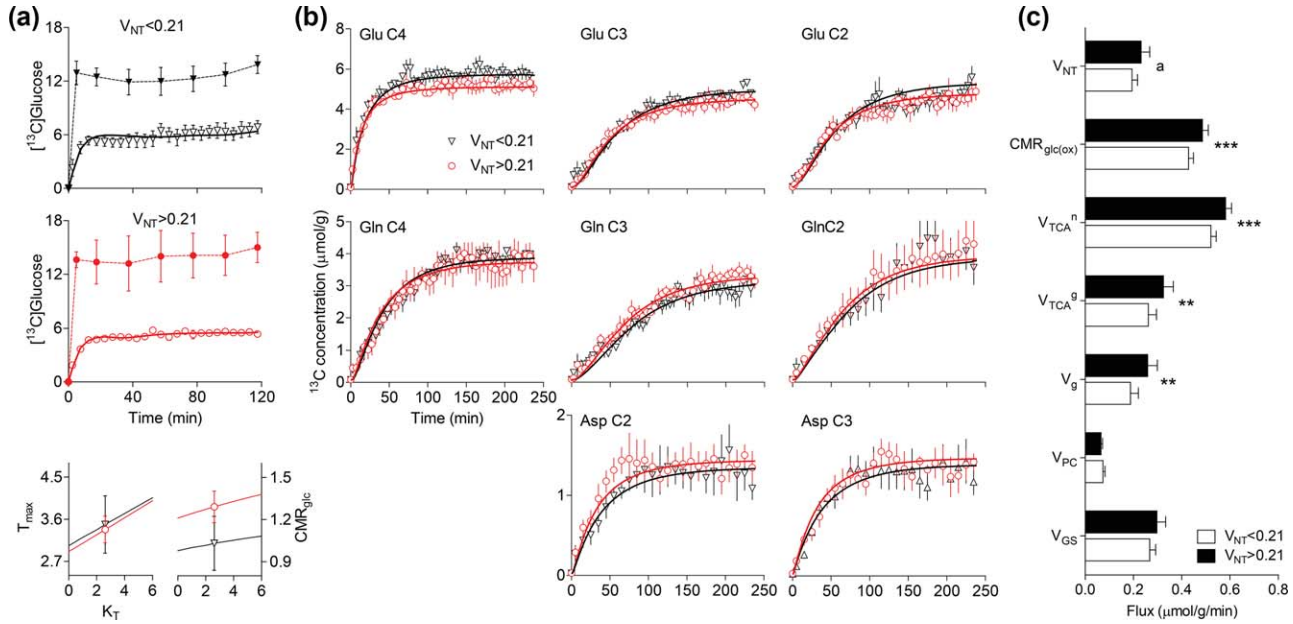

FIGURE 5 Analysis of ^{13}C curves averaged over the tree shrews in Group A ($V_{NT} < 0.21$ μmol/g/min) and Group B ($V_{NT} > 0.21$ μmol/g/min). (a) Analysis of [^{13}C]glucose in the cortex (in μmol/g, open symbols) as function of plasma [^{13}C]glucose (in mmol/L, filled symbols) during the first 2 hr of glucose infusion. The best fit of the model is represented by the solid line over cortical [^{13}C]glucose. The bottom graphs show the estimated T_{max} and CMR_{glc} for Groups A (black symbols) and B (red symbols) with K_t fixed at 2.6 mmol/L. Analysis of K_t effect on T_{max} and CMR_{glc} is depicted by the solid line. (b) Average ^{13}C enrichment curves (in μmol/g) of aliphatic carbons of glutamate, glutamine, and aspartate (symbols), and best fit of the two-compartment model of brain energy metabolism (lines). (c) Fluxes for energy metabolism pathways and glutamate–glutamine cycle. Data are mean ± *SEM* of $n = 4$, and fluxes (in μmol/g/min) are shown with *SD*; $^{**}p < 0.01$, $^{***}p < 0.001$, $^{a}p = 0.013$ before correction for multiple comparisons [Color figure can be viewed at wileyonlinelibrary.com]

shrew, and exhibit a coupling between oxidative metabolism and glutamatergic neurotransmission, depicted by V_{NT}.

To allow visual stimulation in small animals for prolonged periods, we applied a stimulation paradigm that consisted of moving lines with random variation of orientation, direction and temporal frequency, which likely excites distinct neuron subpopulations (Bosking *et al*., 2002; Van Hooser *et al*., 2013), and allows minimizing habituation to continuous stimuli and desensitization of neuronal and hemodynamic responses (Sonnay *et al*., 2015 and references therein). With our protocol, a metabolic steady-state is not reached at single cell level. However, with randomly switched stimuli every 5 sec, this may be negligible within the whole cortical tissue during prolonged stimulation.

Metabolic flux analysis with ^{13}C MRS data was performed in two distinct ways, both pointing towards an increase in oxidative metabolism during V_{NT} stimulation. Namely, the model was firstly fitted to the ^{13}C labeling curves obtained from each tree shrew, which provided insight into the biological variability of the metabolic fluxes (Figure 4). Most importantly, this analysis permitted to evaluate the relationship between fluxes of oxidative metabolism and V_{NT}. Then, experiments were split in low and high V_{NT}, and metabolic fluxes were determined by fitting the model to ^{13}C curves averaged over four tree shrews per group (Figure 5). This analysis allows reducing the influence of experimental uncertainty on model fitting, and thus increase the reliability of estimated parameters. Additionally, since the present modeling

TABLE 2 Metabolic fluxes (in μmol/g/min) obtained from fitting Groups A ($V_{NT} < 0.21$) and B ($V_{NT} > 0.21$), and respective *p* values obtained with two-tailed Student *t* test after permutation analysis and correction for multiple comparisons. Fluxes are shown with associated *SD* estimated from Monte-Carlo simulations

	A: $V_{NT} < 0.21$	B: $V_{NT} > 0.21$	*p* Value
Measured:			
V_{NT}	0.19 ± 0.02	0.23 ± 0.04	0.090[a]
V_{TCA}^n	0.52 ± 0.02	0.58 ± 0.02	<0.001
V_{TCA}^g	0.26 ± 0.03	0.32 ± 0.04	0.010
V_{PC}	0.07 ± 0.01	0.07 ± 0.01	>0.1
V_X^n	4.51 ± 4.47[§]	5.30 ± 4.98[§]	>0.1
V_X^g	0.31 ± 0.39[§]	1.09 ± 1.59[§]	>0.1
V_{dil}	0.13 ± 0.02	0.21 ± 0.06	0.002
V_{ex}	0.05 ± 0.06[§]	0.06 ± 0.06[§]	>0.1
V_{in}	0.00 ± 0.00	0.06 ± 0.04	<0.001
T_{max}	3.49 ± 0.61	3.39 ± 0.29	>0.1
CMR_{glc}	1.03 ± 0.19	1.29 ± 0.11	0.009
Calculated:			
V_g	0.19 ± 0.03	0.26 ± 0.04	0.002
V_{GS}	0.27 ± 0.02	0.30 ± 0.04	>0.1
V_{out}	1.21 ± 0.39	1.68 ± 0.23	0.086[b]
$CMR_{glc(ox)}$	0.43 ± 0.02	0.49 ± 0.02	<0.001

[a]$p = 0.013$ and [b]$p = 0.011$ before correction. [§]For histograms with long tails (V_{ex},V_X^n, and V_X^g), *SD* calculation excluded histogram values that were 10-fold above the estimated flux value. For V_X^g in Group B, we kept 80% of all values. The remaining cases were above 95%.

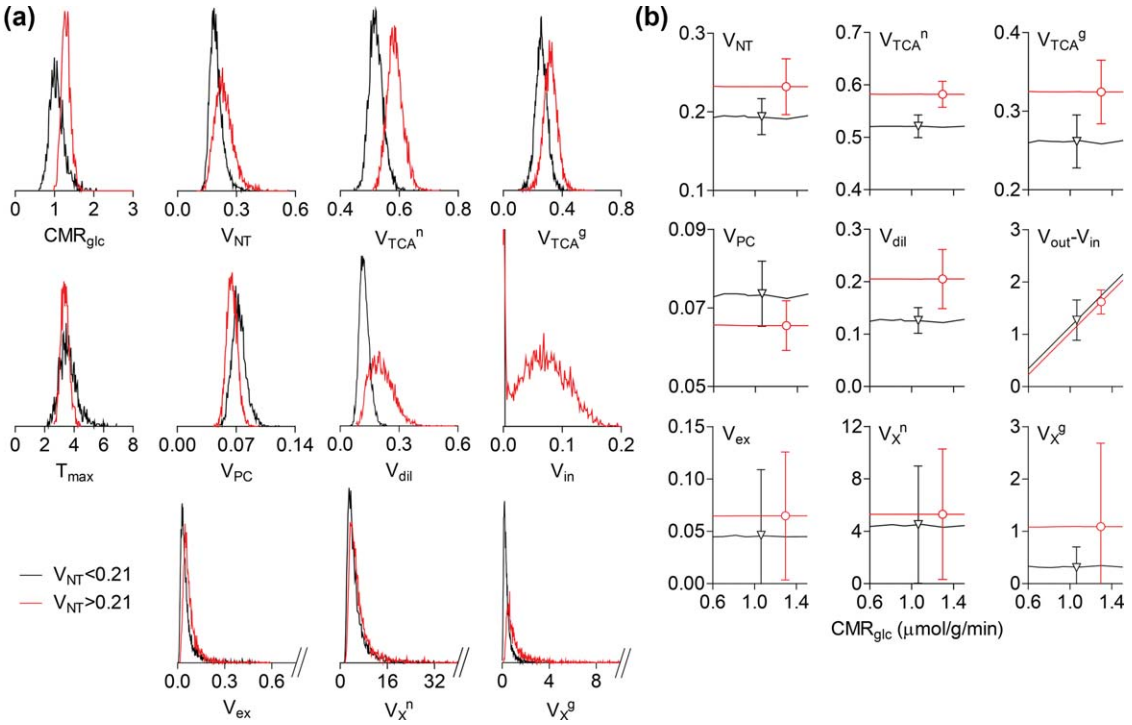

FIGURE 6 (a) Probability distribution of the estimated fluxes resulting from the Monte-Carlo analysis. (b) Effect of CMR_{glc} on the estimation of the metabolic fluxes (in μmol/g/min). Symbols depict the determined fluxes (with *SD*). Black and red traces depict Groups A ($V_{NT} < 0.21$ μmol/g/min) and B ($V_{NT} > 0.21$ μmol/g/min), respectively [Color figure can be viewed at wileyonlinelibrary.com]

approach requires knowledge of brain metabolic pools, ^{1}H MRS was performed to measure the concentration of cortical metabolites at rest and during visual stimulation. Noteworthy, ^{1}H and ^{13}C experiments provided complementary information regarding the stimulation-induced impact on glucose metabolism.

We measured for the first time the neurochemical profile in the tree shrew cortex by means of ^{1}H MRS *in vivo*. In contrast to rodents and humans (Duarte & Gruetter, 2012), we noted that alanine and ascorbate were undetectable in the tree shrew V1. Thus, a neurochemical profile composed of 16 metabolites was measured over baseline (rest), stimulation and recovery periods (acquisition during ~1 hr), from a VOI within the area of intense activation, as detected *a priori* by BOLD fMRI.

Stimulation-induced increase of cortical activity resulted in a reduction of glucose concentration, which recovered to baseline levels after visual stimulation. The magnitude of glucose change in this study (−0.34 μmol/g) is consistent with previous studies in the human visual cortex, in which the decrease in glucose levels ranged from 0.2 to 0.4 μmol/g (Bednařík *et al*., 2015; Lin, Stephenson, Xin, Napolitano, & Morris, 2012; Mangia *et al*., 2007; Schaller, Mekle, Xin, Kunz, & Gruetter, 2013). This glucose reduction reflects increased glucose utilization (*e.g*., Collins, McCandless, & Wagman, 1987; Cruz *et al*., 2005; Sonnay *et al*., 2016) relative to the rate of glucose uptake from circulation, as confirmed by ^{13}C MRS. Indeed, the ratio T_{max}/CMR_{glc} that is indicative of brain glucose levels at a given plasma glucose (see Duarte & Gruetter, 2012) was larger at rest than upon stimulation (3.7 vs. 3.0). Similar calculations using results from fitted average [^{13}C]glucose curves indicate a decrease in T_{max}/CMR_{glc} from 3.4 to 2.6 for a 20% increase in V_{NT} (from Groups A to B).

TABLE 3 Age, gender and ^{13}C MRS experiment characteristics for each of the tree shrews in the study. Animal numbering is as in Figure 4

			^{13}C MRS experiment	
Animal #	Age (years)	Gender	Protocol	Duration (min)
1	3.8	Female	Stimulation	240
2	5.5	Female	Stimulation	160
3	6.6	Female	Stimulation	250
4	4.8	Female	Rest	250
5	5.0	Female	Rest	230
6	1.4	Female	Stimulation	250
7	0.6	Male	Rest	250
8	0.5	Male	Stimulation	250
9	0.6	Female	Rest	250

TABLE 4 Distribution of age and gender across experimental groups

	Age (years)		
	Range	mean ± *SEM*	Gender (male:female)
Rest	0.6 – 5.0	2.8 ± 1.2	1:3
Stimulation	0.5 – 6.6	3.6 ± 1.2	1:4
Group A	0.6 – 5.0	3.0 ± 1.1	1:3
Group B	0.5 – 6.6	2.9 ± 1.5	1:3

A T_{max} larger than CMR_{glc} suggests that glucose transport is not limiting for its metabolism under physiological conditions, that is euglycemia and above. In this study, T_{max} was similar for low and high V_{NT} groups. Therefore, reduced cortical glucose in the absence of plasma glucose changes leads to stimulation of net glucose uptake (T_{net}) by the cortex. More precisely, we estimated that stimulation of V_{NT} was associated with an increase of net glucose uptake of 0.19 μmol/g/min (+14% for Group B *vs.* A) at a steady-state plasma glucose of 7 mmol/L (Table 1) and the measured change in cortical glucose content (Figure 2). This T_{net} increase is slightly smaller than the measured increase in glucose consumption (ΔCMR_{glc} = 0.26 μmol/g/min), thus resulting in a reduction of cortical glucose until a new steady-state is reached. In the time course of cortical glucose measured by ^{1}H MRS, the novel glucose steady-state is achieved after 15 min of stimulation, although fluxes of glucose uptake and consumption likely change much faster upon switching neuronal activity (Barros, Bittner, Loaiza, & Porras, 2007).

The remarkable decrease in the PCr/Cr ratio measured during stimulation was also reported previously (Chen, Zhu, Adriany, & Ugurbil, 1997; Xu, Yang, Li, Zhu, & Shen, 2005). Creatine is mainly phosphorylated in mitochondria, incorporating therefore the high energy phosphate produced by oxidative phosphorylation, and the newly synthetized phosphocreatine is shuttled to the cytosol, where it constitutes a readily available source of energy (Wallimann, Tokarska-Schlattner, & Schlattner, 2011). A shift towards adenosine triphosphate (ATP) synthesis from phosphocreatine can be stimulated by increased adenosine diphosphate (ADP) production during enhanced neuronal activity (Chen *et al*., 1997). Increased rate of ADP production further stimulates oxidative metabolism. Indeed, visual stimulation robustly induced an increase in the rate of oxidative metabolism in both neurons (V_{TCA}^n) and astrocytes (V_{TCA}^g).

In both Groups A and B, CMR_{glc} was larger than $CMR_{glc(ox)}$, which implies a net efflux of pyruvate or other glucose metabolites from the cortical parenchyma. This discordance between total and oxidative glucose metabolism *in vivo* is known as aerobic glycolysis, that is, the fraction of glycolysis that does not convert glucose to CO_2 when O_2 levels and supply are adequate. With increased V_{NT} there was also a trend for increased net pyruvate loss (V_{out}–V_{in}) of 0.41 μmol/g/min (within uncertainty), which is consistent with evidence for large increases in glycolysis associated with rapid release of labeled glucose-derived metabolites from the activated tissue (*e.g*., Collins *et al*., 1987), which is ascribed to lactate efflux (Dienel & Cruz, 2003). Interestingly, we observed an increase in V_{in} with increased neurotransmission despite the large increase in the net pyruvate efflux. Furthermore, with increasing V_{TCA}^g there was also an increase in V_{dil}, indicative of dilution of astrocytic TCA cycle precursors by unlabeled substrates. The increase in V_{in} and V_{dil} suggests that substrates other than glucose are utilized in the activated cortex.

Small increases in cortical lactate concentration (ranging from 0.1 to 0.3 μmol/g) have been reported during stimulation in the human cortex (Bednařík *et al*., 2015; Lin *et al*., 2012; Mangia *et al*., 2007; Schaller *et al*., 2013). In rats under light α-chloralose anesthesia, we have previously reported lactate increases of 0.8–1 μmol/g in the rat barrel cortex upon trigeminal nerve stimulation (Just, Xin, Frenkel, & Gruetter, 2013; Sonnay *et al*., 2017a). Since we did not observe a modification of lactate concentration in the cortex during stimulation, we speculate that its extrusion from the activated tissue might also increase in the conditions of our study. This glycolysis-derived lactate can be oxidized (Duarte *et al*., 2015 and references therein) or released into the blood stream (Cruz *et al*., 1999; Dienel & Cruz, 2003). Absence of lactate changes in the stimulated cortex were also reported in humans (Boucard *et al*., 2005) and rats (Xu *et al*., 2005). Noteworthy, the methyl protons of lactate, which are the most prominent resonance in the ^{1}H spectrum (at ∼1.3 ppm), may be particularly affected by extra-cerebral lipid contamination. In spite of pancuronium bromide administration to prevent animal movements, and a VOI position that avoids signal from extra-cerebral fat tissue, lipid contamination cannot be fully excluded.

At low V_{NT}, V_{TCA}^g was about half of V_{TCA}^n. Since the nominal increase was similar for both fluxes, the relative increase of the TCA cycle rate with increasing V_{NT} was much larger in astrocytes than in neurons. Namely, the V_{TCA}^g fraction of total oxidative metabolism was 33% and 36% in Groups A and B, respectively. In contrast, V_{PC} did not increase with V_{NT}, and while it accounted for 28% of V_{TCA}^g in Group A, it was only 20% in Group B. V_{PC} is required for *de novo* amino acid synthesis in the brain, and thus the lack of stimulation-induced V_{PC} increase is in line with no major change in glutamate measured in the present study by ^{1}H MRS. The absence of glutamate changes, however, contrasts with previous reports in the rodent and human cortex (Bednařík *et al*., 2015; Just *et al*., 2013; Lin *et al*., 2012; Mangia *et al*., 2007; Schaller *et al*., 2013). Interestingly, lack of V_{PC} increase was also found in a previous study in the rat cortex (Sonnay *et al*., 2016) and during bicuculline-seizures (Patel *et al*., 2005), which induce acute shifts in neuronal activity. On the other hand, V_{PC} was found larger in awake than anesthetized rats (Oz *et al*., 2014), and it appears to decrease with anesthesia depth (discussed in Lanz *et al*., 2013). In addition to the lack of V_{PC} changes, oxidation of glutamate in astrocytes (possible through V_X) can contribute to prevent its accumulation upon increased neuronal activity (Hertz & Hertz, 2003; Nissen *et al*., 2015; Sonnewald, Westergaard, & Schousboe, 1997). Astrocytic processes enveloping synaptic terminals contain large amounts of glutamate dehydrogenase and mitochondria that allow glutamate catabolism (Karaca *et al*., 2015). Moreover their glutamate transporters are physically and/or functionally coupled to Na^+/K^+-ATPase, Na^+/Ca^{2+} exchanger, glycogen phosphorylase, glycolytic enzymes, and several mitochondrial proteins, promoting therefore an efficient regulation of energy metabolism (Robinson & Jackson, 2016).

In neurons, the increased energy production upon enhanced cortical activity is likely used for restoration of ion gradients caused by action potentials, for postsynaptic currents, for neurotransmitter packing and for Ca^{2+} homeostasis (Attwell & Laughlin, 2001; Ferragamo, Reinardy, & Thayer, 2009). In astrocytes, the increase in ATP production by the TCA cycle appears to be much larger than the requirements of the increased glutamate-glutamine cycle rate *per se* (for glutamate uptake and glutamine synthesis). While fueling glutamate uptake and glutamine synthetase activity is fundamental for glutamatergic neurotransmission (Trabelsi, Amri, Becq, Molinari, & Anikstejn, 2017), it has been proposed that handling of K^+ uptake accounts for a large fraction of

astrocytic energy consumption, especially at high neurotransmission rates (DiNuzzo, Giove, Maraviglia, & Mangia, 2017). Moreover, energy produced in astrocytes might fuel the production of neuromodulators, vasoactive compounds, and antioxidant molecules (reviewed in Sonnay *et al*., 2017c).

One caveat of this study is the utilization of animals with varied age (0.5–6.6 years), although tree shrews reach adulthood at the age of 2 months and have up to 12 years lifespan in captivity (Fuchs & Corbach-Söhle, 2010). Cerebral glucose utilization is known to be reduced with aging (Gage, Kelly, & Björklund, 1984; Tack, Wree, & Schleicher, 1989), and a ^{13}C MRS study also found reduced $V_{TCA}{}^{n}$ in elderly *versus* young subjects (Boumezbeur *et al*., 2010). From all fluxes estimated with our model, only $V_{TCA}{}^{n}$ correlated with age, and this age-associated decline in $V_{TCA}{}^{n}$ might explain why this flux was not found significantly increased in the single animal analysis.

Upon modulation of brain activity by administration of different anesthetics, Sibson *et al*. (1998) found that the rates of glucose metabolism and the glutamate–glutamine cycle are stoichiometrically coupled from isoelectricity ($V_{NT} = 0$) to $V_{NT} \sim 0.5$ μmol/g/min. Similar correlation analyses have been performed by pooling data obtained in a variety of experimental conditions (*e.g*., Hyder & Rothman, 2012; Lanz *et al*., 2013). However, anesthetics not only modulate basal neuronal activity, but also the coupling between neuronal activity and vascular regulation (Masamoto & Kanno, 2012), and may differently impact the relative rates of glucose oxidation within neurons and astrocytes (Sonnay *et al*., 2017b). While the present study has a narrower range of V_{NT} values for correlation analysis (0.13–0.26 μmol/g/min), it has the advantage that anesthesia and physiology of the animals were identical across all animals studied.

In sum, from the relationship of energy metabolism fluxes to a surrogate of cortical activity, V_{NT}, we conclude that variations of neuronal and astrocytic oxidative metabolism were of similar amplitude and coupled to the rate of glutamate–glutamine cycle (V_{NT}), and that increases in ATP production in astrocytes extend beyond the immediate needs of glutamate recycling.

ACKNOWLEDGMENT

This research was supported by the Swiss National Science Foundation (grants 148250 to J. M. N. D., and 149983 to R. G.), National Competence Center in Biomedical Imaging (NCCBI), and by Centre d'Imagerie BioMédicale (CIBM) of the UNIL, UNIGE, HUG, CHUV, EPFL and the Leenaards and Jeantet Foundations. The authors thank Jaquelina Romero and Yves Pilloud for technical support. The authors declare the absence of potential conflicts of interest.

ORCID

João M.N. Duarte http://orcid.org/0000-0001-5984-1574

REFERENCES

Amaral, A. I., Hadera, M. G., Tavares, J. M., Kotter, M. R., & Sonnewald, U. (2016). Characterization of glucose-related metabolic pathways in differentiated rat oligodendrocyte lineage cells. *Glia*, *64*(1), 21–34.

Attwell, D., & Laughlin, S. B. (2001). An energy budget for signaling in the grey matter of the brain. *The Journal of Cerebral Blood Flow & Metabolism*, *21*, 1133–1145.

Barros, L. F., Bittner, C. X., Loaiza, A., & Porras, O. H. (2007). A quantitative overview of glucose dynamics in the gliovascular unit. *Glia*, *55* (12), 1222–1237.

Bednařík, P., Tkáč, I., Giove, F., DiNuzzo, M., Deelchand, D., Emir, U., … Mangia, S. (2015). Neurochemical and BOLD responses during neuronal activation measured in the human visual cortex at 7 Tesla. *The Journal of Cerebral Blood Flow & Metabolism*, *35*(4), 601–610.

Bosking, W., Crowley, J., & Fitzpatrick, D. (2002). Spatial coding of position and orientation in primary visual cortex. *Nature Neuroscience*, *5* (9), 874–882.

Boucard, C., Mostert, J., Cornelissen, F., De Keyser, J., Oudkerk, M., & Sijens, P. (2005). Visual stimulation, 1H MR spectroscopy and fMRI of the human visual pathways. *European Radiology*, *15*(1), 47–52.

Boumezbeur, F., Mason, G. F., de Graaf, R. A., Behar, K. L., Cline, G. W., Shulman, G. I., … Petersen, K. F. (2010). Altered brain mitochondrial metabolism in healthy aging as assessed by in vivo magnetic resonance spectroscopy. *The Journal of Cerebral Blood Flow & Metabolism*, *30*(1), 211–221.

Chen, W., Zhu, X., Adriany, G., & Ugurbil, K. (1997). Increase of creatine kinase activity in the visual cortex of human brain during visual stimulation: A ^{31}P magnetization transfer study. *Magnetic Resonance in Medicine*, *38*(4), 551–557.

Chuquet, J., Quilichini, P., Nimchinsky, E. A., & Buzsáki, G. (2010). Predominant enhancement of glucose uptake in astrocytes versus neurons during activation of the somatosensory cortex. *Journal of Neuroscience*, *30*, 15298–15303.

Collins, R., McCandless, D., & Wagman, I. (1987). Cerebral glucose utilization: Comparison of [^{14}C]deoxyglucose and [6-^{14}C]glucose quantitative autoradiography. *Journal of Neurochemistry*, *49*(5), 1564–1570.

Cruz, N. F., Adachi, K., & Dienel, G. A. (1999). Rapid efflux of lactate from cerebral cortex during K^{+}-induced spreading cortical depression. *The Journal of Cerebral Blood Flow & Metabolism*, *19*(4), 380–392.

Cruz, N. F., Lasater, A., Zielke, H. R., & Dienel, G. A. (2005). Activation of astrocytes in brain of conscious rats during acoustic stimulation: Acetate utilization in working brain. *Journal of Neurochemistry*, *92*(4), 934–947.

Dienel, G. A., & Cruz, N. F. (2003). Neighborly interactions of metabolically-activated astrocytes *in vivo*. *Neurochemistry International*, *43*(4–5), 339–354.

Dienel, G. A., Schmidt, K. C., & Cruz, N. F. (2007). Astrocyte activation *in vivo* during graded photic stimulation. *Journal of Neurochemistry*, *103* (4), 1506–1522.

DiNuzzo, M., Giove, F., Maraviglia, B., & Mangia, S. (2017). Computational flux balance analysis predicts that stimulation of energy metabolism in astrocytes and their metabolic interactions with neurons depend on uptake of K+ rather than glutamate. *Neurochemistry Research*, *42*(1), 202–216.

Drenhaus, U., Rager, G., Eggli, P., & Kretz, R. (2006). On the postnatal development of the striate cortex (V1) in the tree shrew (*Tupaia belangeri*). *European Journal of Neuroscience*, *24*(2), 479–490.

Duarte, J. M. N., Cunha, R., & Carvalho, R. (2007). Different metabolism of glutamatergic and GABAergic compartments in superfused hippocampal slices characterized by nuclear magnetic resonance spectroscopy. *Neuroscience*, *144*(4), 1305–1313.

Duarte, J. M. N., Do, K. Q., & Gruetter, R. (2014). Longitudinal neurochemical modifications in the aging mouse brain measured *in vivo* by ^{1}H magnetic resonance spectroscopy. *Neurobiology of Aging*, *35*(7), 1660–1668.

Duarte, J. M. N., Girault, F.-M., & Gruetter, R. (2015). Brain energy metabolism measured by ^{13}C MRS *in vivo* upon infusion of [3-^{13}C] lactate. *Journal of Neuroscience Research*, *93*(7), 1009–1018.

Duarte, J. M. N., & Gruetter, R. (2012). Characterization of cerebral glucose dynamics *in vivo* with a four-state conformational model of transport at the blood–brain barrier. *Journal of Neurochemistry*, *121* (3), 396–406.

Duarte, J. M. N., & Gruetter, R. (2013). Glutamatergic and GABAergic energy metabolism measured in the rat brain by ^{13}C NMR spectroscopy at 14.1 T. *Journal of Neurochemistry*, *126*(5), 579–590.

Duarte, J. M. N., Lanz, B., & Gruetter, R. (2011). Compartmentalised cerebral metabolism of [1,6-^{13}C]glucose determined by *in vivo* ^{13}C NMR spectroscopy at 14.1 T. *Frontiers in Neuroenergetics*, *3*, 3.

Duarte, J. M. N., Lei, H., Mlynárik, V., & Gruetter, R. (2012). The neurochemical profile quantified by *in vivo* ^{1}H NMR spectroscopy. *NeuroImage*, *61*(2), 342–362.

Ferragamo, M., Reinardy, J., & Thayer, S. (2009). Ca^{2+}-dependent, stimulus-specific modulation of the plasma membrane Ca^{2+} pump in hippocampal neurons. *Journal of Neurophysiology*, *101*(5), 2563–2571.

Fuchs, E., & Corbach-Söhle, S. (2010). Tree Shrews. In R. Hubrecht, & J Kirkwood (Eds.), *The UFAW Handbook on the Care and Management of Laboratory and Other Research Animals*. (pp. 262–275). Oxford, UK: Wiley-Blackwell.

Gage, F. H., Kelly, P. A., & Björklund, A. (1984). Regional changes in brain glucose metabolism reflect cognitive impairments in aged rats. *Journal of Neuroscience*, *4*, 2856–2865.

Gordon, G., Choi, H., Rungta, R., Ellis-Davies, G., & MacVicar, B. (2008). Brain metabolism dictates the polarity of astrocyte control over arterioles. *Nature*, *456*(7223), 745–749.

Gruetter, R., & Tkác, I. (2000). Field mapping without reference scan using asymmetric echo-planar techniques. *Magnetic Resonance in Medicine*, *43*(2), 319–323.

Henry, P. G., Oz, G., Provencher, S., & Gruetter, R. (2003b). Toward dynamic isotopomer analysis in the rat brain *in vivo*: Automatic quantitation of ^{13}C NMR spectra using LCModel. *NMR in Biomedicine*, *16*, 400–412.

Henry, P. G., Tkác, I., & Gruetter, R. (2003a). ^{1}H-localized broadband ^{13}C NMR spectroscopy of the rat brain *in vivo* at 9.4 T. *Magnetic Resonance in Medicine*, *50*, 684–692.

Hertz, L., & Hertz, E. (2003). Cataplerotic TCA cycle flux determined as glutamate-sustained oxygen consumption in primary cultures of astrocytes. *Neurochemistry International*, *43*(4–5), 355–361.

Hyder, F., Chase, J. R., Behar, K. L., Mason, G. F., Siddeek, M., Rothman, D. L., & Shulman, R. G. (1996). Increased tricarboxylic acid cycle flux in rat brain during forepaw stimulation detected with ^{1}H[^{13}C]NMR. *Proceedings of the National Academy of Sciences of the United States of America*, *93*, 7612–7617.

Hyder, F., & Rothman, D. L. (2012). Quantitative fMRI and oxidative neuroenergetics. *NeuroImage*, *62*(2), 985–994.

Hyder, F., Rothman, D. L., Mason, G. F., Rangarajan, A., Behar, K. L., & Shulman, R. G. (1997). Oxidative glucose metabolism in rat brain during single forepaw stimulation: A spatially localized ^{1}H[^{13}C] nuclear magnetic resonance study. *The Journal of Cerebral Blood Flow & Metabolism*, *17*, 1040–1047.

Just, N., Xin, L., Frenkel, H., & Gruetter, R. (2013). Characterization of sustained BOLD activation in the rat barrel cortex and neurochemical consequences. *NeuroImage*, *74*, 343–351.

Karaca, M., Frigerio, F., Migrenne, S., Martin-Levilain, J., Skytt, D., Pajecka, K., … Maechler, P. (2015). GDH-dependent glutamate oxidation in the brain dictates peripheral energy substrate distribution. *Cell Reports*, *13*(2), 365–375.

Kim, T., Hendrich, K., Masamoto, K., & Kim, S. (2007). Arterial versus total blood volume changes during neural activity-induced cerebral blood flow change: Implication for BOLD fMRI. *The Journal of Cerebral Blood Flow & Metabolism*, *27*(6), 1235–1247.

Lanz, B., Gruetter, R., & Duarte, J. M. N. (2013). Metabolic flux and compartmentation analysis in the brain *in vivo*. *Frontiers in Endocrinology*, *4*, 156.

Liang, C., Ances, B., Perthen, J., Moradi, F., Liau, J., Buracas, G., … Buxton, R. (2013). Luminance contrast of a visual stimulus modulates the BOLD response more than the cerebral blood flow response in the human brain. *NeuroImage*, *64*, 104–111.

Lin, Y., Stephenson, M., Xin, L., Napolitano, A., & Morris, P. (2012). Investigating the metabolic changes due to visual stimulation using functional proton magnetic resonance spectroscopy at 7 T. *The Journal of Cerebral Blood Flow & Metabolism*, *32*(8), 1484–1495.

Mangia, S., Tkác, I., Gruetter, R., Van de Moortele, P. F., Maraviglia, B., & Uğurbil, K. (2007). Sustained neuronal activation raises oxidative metabolism to a new steady-state level: Evidence from ^{1}H NMR spectroscopy in the human visual cortex. *The Journal of Cerebral Blood Flow & Metabolism*, *27*, 1055–1063.

Masamoto, K., & Kanno, I. (2012). Anesthesia and the quantitative evaluation of neurovascular coupling. *The Journal of Cerebral Blood Flow & Metabolism*, *32*(7), 1233–1247.

Mlynárik, V., Gambarota, G., Frenkel, H., & Gruetter, R. (2006). Localized short-echo-time proton MR spectroscopy with full signal-intensity acquisition. *Magnetic Resonance in Medicine*, *56*, 965–970.

Nissen, J. D., Pajęcka, K., Stridh, M. H., Skytt, D. M., & Waagepetersen, H. S. (2015). Dysfunctional TCA-cycle metabolism in glutamate dehydrogenase deficient astrocytes. *Glia*, *63*(12), 2313–2326.

Norton, T., Wu, W., & Siegwart, J. J. (2003). Refractive state of tree shrew eyes measured with cortical visual evoked potentials. *Optometry and Vision Science*, *80*(9), 623–631.

Oz, G., Berkich, D. A., Henry, P. G., Xu, Y., LaNoue, K., Hutson, S. M., & Gruetter, R. (2014). Neuroglial metabolism in the awake rat brain: CO_2 fixation increases with brain activity. *Journal of Neuroscience*, *24* (50), 11273–11279.

Patel, A. B., Chowdhury, G. M., de Graaf, R. A., Rothman, D. L., Shulman, R. G., & Behar, K. L. (2005). Cerebral pyruvate carboxylase flux is unaltered during bicuculline-seizures. *Journal of Neuroscience Research*, *79*(1–2), 128–138.

Robinson, M. B., & Jackson, J. G. (2016). Astroglial glutamate transporters coordinate excitatory signaling and brain energetics. *Neurochemistry International*, *98*, 56–71.

Schaller, B., Mekle, R., Xin, L., Kunz, N., & Gruetter, R. (2013). Net increase of lactate and glutamate concentration in activated human visual cortex detected with magnetic resonance spectroscopy at 7 tesla. *Journal of Neuroscience Research*, *91*(8), 1076–1083.

Sesma, M., Casagrande, V., & Kaas, J. (1984). Cortical connections of area 17 in tree shrews. *The Journal of Comparative Neurology*, *230*(3), 337–351.

Sibson, N., Dhankhar, A., Mason, G., Rothman, D., Behar, K., & Shulman, R. (1998). Stoichiometric coupling of brain glucose metabolism and glutamatergic neuronal activity. *Proceedings of the National Academy of Sciences of the United States of America*, *95*(1), 316–321.

Sonnay, S., Duarte, J. M. N., & Just, N. (2017a). Lactate and Glutamate dynamics during prolonged stimulation of the rat barrel cortex suggest adaptation of cerebral glucose and oxygen metabolism. *Neuroscience*, *346*, 337–348.

Sonnay, S., Duarte, J. M. N., Just, N., & Gruetter, R. (2016). Compartmentalised energy metabolism supporting glutamatergic neurotransmission

in response to increased activity in the rat cerebral cortex: A ^{13}C MRS study *in vivo* at 14.1 T. *The Journal of Cerebral Blood Flow & Metabolism*, *36*(5), 928–940.

Sonnay, S., Duarte, J. M. N., Just, N., & Gruetter, R. (2017b). Energy metabolism in the rat cortex under thiopental anaesthesia measured *in vivo* by ^{13}C MRS. *Journal of Neuroscience Research*, in press. https://doi.org/10.1002/jnr.24032.

Sonnay, S., Gruetter, R., & Duarte, J. M. N. (2017c). How energy metabolism supports cerebral function: Insights from ^{13}C magnetic resonance studies *in vivo*. *Frontiers in Neuroscience*, *11*, 288.

Sonnay, S., Just, N., Duarte, J. M. N., & Gruetter, R. (2015). Imaging of prolonged BOLD response in the somatosensory cortex of the rat. *NMR in Biomedicine*, *28*(3), 414–421.

Sonnewald, U., Westergaard, N., & Schousboe, A. (1997). Glutamate transport and metabolism in astrocytes. *Glia*, *21*(1), 56–63.

Strupp, J. (1996). Stimulate a GUI based fMRI analysis software package. *NeuroImage*, *3*, S607.

Tack, W., Wree, A., & Schleicher, A. (1989). Local cerebral glucose utilization in the hippocampus of old rats. *Histochemistry*, *92*, 413–419.

Trabelsi, Y., Amri, M., Becq, H., Molinari, F., & Aniksztejn, L. (2017). The conversion of glutamate by glutamine synthase in neocortical astrocytes from juvenile rat is important to limit glutamate spillover and peri/extrasynaptic activation of NMDA receptors. *Glia*, *65*(2), 401–415.

Van Hooser, S., Roy, A., Rhodes, H., Culp, J. H., & Fitzpatrick, D. (2013). Transformation of receptive field properties from lateral geniculate nucleus to superficial V1 in the tree shrew. *Journal of Neuroscience*, *33*(28), 11494–11505.

Veit, J., Bhattacharyya, A., Kretz, R., & Rainer, G. (2011). Neural response dynamics of spiking and local field potential activity depend on CRT monitor refresh rate in the tree shrew primary visual cortex. *Journal of Neurophysiology*, *106*(5), 2303–2313.

Veit, J., Bhattacharyya, A., Kretz, R., & Rainer, G. (2014). On the relation between receptive field structure and stimulus selectivity in the tree shrew primary visual cortex. *Cerebral Cortex*, *24*(10), 2761–2771.

Volterra, A., & Meldolesi, J. (2005). Astrocytes, from brain glue to communication elements: The revolution continues. *Nature Reviews Neuroscience*, *6*(8), 626–640.

Wallimann, T., Tokarska-Schlattner, M., & Schlattner, U. (2011). The creatine kinase system and pleiotropic effects of creatine. *Amino Acids*, *40*(5), 1271–1296.

Xu, S., Yang, J., Li, C., Zhu, W., & Shen, J. (2005). Metabolic alterations in focally activated primary somatosensory cortex of α-chloralose-anesthetized rats measured by ^{1}H MRS at 11.7 T. *NeuroImage*, *28*(2), 401–409.

Yang, J., & Shen, J. (2006). Increased oxygen consumption in the somatosensory cortex of alpha-chloralose anesthetized rats during forepaw stimulation determined using MRS at 11.7 Tesla. *NeuroImage*, *32*, 1317–1325.

How to cite this article: Sonnay S, Poirot J, Just N, et al. Astrocytic and neuronal oxidative metabolism are coupled to the rate of glutamate–glutamine cycle in the tree shrew visual cortex. *Glia*. 2018;66:477–491. https://doi.org/10.1002/glia.23259